Large-scale modes of turbulent channel flow: transport and structure

By Z. LIU[1,2], R. J. ADRIAN[1] AND T. J. HANRATTY[2]

[1]Laboratory for Turbulence and Complex Flow, Department of Theoretical and
Applied Mechanics, University of Illinois, Urbana, IL 61801, USA

[2]Department of Chemical Engineering, University of Illinois, Urbana, IL 61801, USA

Turbulent flow in a rectangular channel is investigated to determine the scale and pattern of the eddies that contribute most to the total turbulent kinetic energy and the Reynolds shear stress. Instantaneous, two-dimensional particle image velocimeter measurements in the streamwise-wall-normal plane at Reynolds numbers $Re_h = 5378$ and 29 935 are used to form two-point spatial correlation functions, from which the proper orthogonal modes are determined. Large-scale motions – having length scales of the order of the channel width and represented by a small set of low-order eigenmodes – contain a large fraction of the kinetic energy of the streamwise velocity component and a small fraction of the kinetic energy of the wall-normal velocities. Surprisingly, the set of large-scale modes that contains half of the total turbulent kinetic energy in the channel, also contains two-thirds to three-quarters of the total Reynolds shear stress in the outer region. Thus, it is the large-scale motions, rather than the main turbulent motions, that dominate turbulent transport in all parts of the channel except the buffer layer. Samples of the large-scale structures associated with the dominant eigenfunctions are found by projecting individual realizations onto the dominant modes. In the streamwise wall-normal plane their patterns often consist of an inclined region of second quadrant vectors separated from an upstream region of fourth quadrant vectors by a stagnation point/shear layer. The inclined Q4/shear layer/Q2 region of the largest motions extends beyond the centreline of the channel and lies under a region of fluid that rotates about the spanwise direction. This pattern is very similar to the signature of a hairpin vortex. Reynolds number similarity of the large structures is demonstrated, approximately, by comparing the two-dimensional correlation coefficients and the eigenvalues of the different modes at the two Reynolds numbers.

1. Introduction

It is implicit in the velocity defect law, and other statements of outer flow similarity for turbulent flow over walls, that large-scale motions scaling with the outer length scale exist in these flows. As in the inner wall-layer, these motions are coherent in the sense that they have characteristic flow patterns that persist over times long enough to contribute significantly to the time average character of the flow. Perhaps the best known large-scale motions are the bulges of the turbulent boundary layer. They travel at approximately 80% of the free-stream velocity, and they are about two boundary-layer thicknesses long and 1–2 boundary-layer thicknesses wide (Kovasznay, Kibens & Blackwelder 1970; Murlis, Tsai & Bradshaw 1982). The low-speed puffs observed

by Wygnanski & Champagne (1973) are another well-known type of large-scale motion that occurs in pipe flow, albeit only at sufficiently low Reynolds numbers and/or with sufficiently smooth entry conditions. Large-scale motions in the form of two-dimensional roll-cells oriented with their rotation axis in the streamwise direction and spanning the width of the flow have been observed in plane turbulent Couette flow; however, in this case the rolls cells appear to be steady and may therefore be better interpreted as secondary flow instabilities of the mean flow (Lee & Kim 1991; Papavassiliou & Hanratty 1997).

Although the low-speed streaks that occur in the buffer layer of wall turbulence have very long dimensions in the streamwise x-direction, their spanwise and wall-normal scales are small, of the order of 100 viscous wall units (Kline *et al.* 1967; Robinson 1991). Therefore, at elevated Reynolds numbers, where the ratio of the outer length scale to the inner viscous length scale is large, near-wall streaks are very thin, and the large-scale motions are distinguished from them by their much larger extent in the wall-normal y-direction and the spanwise z-direction. In the present work, which deals with data in the (x, y)-plane, 'large scale' will denote motions that are large in both the x- and y-directions.

Townsend (1958) and Grant (1958) both observed that the long tail on the streamwise correlation function of the streamwise velocity implied that large-scale motions contribute significantly to the streamwise kinetic energy. Townsend (1958, 1976) argued that the long extent in the x-direction implied small values of the v-component of velocity, and hence small contributions to the Reynolds shear stress, even though the contribution to the kinetic energy of u is large. He termed the large eddies close to the wall 'inactive', and focused attention on the 'main' turbulence eddies which are those with length scales in the inertial range. Several experimental investigations provide spectral data that can be interpreted to support Townsend's view that large-scale motions contain a substantial fraction of the streamwise kinetic energy, cf. Lekakis (1988), for example. A few studies (Naguib & Wark 1992; Adrian & Lekakis 1991) have reported direct observations of this effect.

However, a question exists about the degree to which large-scale motions contribute to the Reynolds shear stress. Using Lekakis' (1988) correlation data, stochastic estimates of $\langle u(t + \tau), v(t + \tau)|u(t), v(t)\rangle$ indicate that after events in which the Reynolds shear stress $u(t)v(t)$ has large values in either the second quadrant (Q2) or fourth quadrant (Q4), there is a rapid transient decay of $\langle u(t + \tau), v(t + \tau)|u(t), v(t)\rangle$ followed by a long time during which the velocity disturbance decays slowly (Adrian & Lekakis 1991). Thus, most of the time that the flow vector spends in the Q2 or Q4 quadrants is due to large time-scale events, i.e. long length-scale motions.

One-dimensional analysis of the type provided by spectral analysis of hot-wire or laser-Doppler velocimetry (LDV) signals is deficient in that it cannot identify the scale of a structure in anything but the mean flow direction. In particular, we cannot distinguish between the contributions from long, thin structures such as near-wall streaks, and the long, thick structures that might occur in the outer region of wall turbulence. Two- or three-dimensional analysis must be used, and for this purpose visualization of two-dimensional particle image velocimetry (PIV) data permits some insights into the large-scale motions in boundary layers (cf. Adrian, Balachandar & Tomkins 1998 and Adrian, Meinhart & Tomkins 2000, for example). The present work is motivated by PIV visualizations in channel flow of large Reynolds stresses associated with large-scale motions having sizes that are, approximately, independent of Reynolds number (Hanratty *et al.* 1993). On average, they had dimensions as large as the channel height in the wall-normal direction and more than two channel heights

in the streamwise direction. Gaussian and spectral sharp-cut filters were used in an attempt to characterize these motions. This approach had a number of disadvantages, in that it could not easily accommodate changes of scale in the wall-normal direction, and a certain amount of subjective judgement entered the analysis.

Proper orthogonal decomposition (POD), a generalization of conventional Fourier power spectral analysis, allows us to evaluate the distribution of energy as a function of scale when the flow is statistically inhomogeneous in one or more directions. It decomposes the vector signal into modes having various scales in each direction, and it evaluates the contribution that each mode makes to the energy and the Reynolds stresses. In the case of channel flow, the modes are trigonometric Fourier modes in the statistically homogeneous streamwise direction, and non-trigonometric in the statistically inhomogeneous wall-normal direction. The POD method is used here to provide a precise and well-defined evaluation of the scales of the motions contributing to both the energy and the stress-producing events from the two-dimensional data.

While the present analysis by POD exclusively addresses the distribution of Reynolds stress as a function of scale, in a manner analogous to Fourier power spectral analysis, it is clear that POD also contains some information about the structure of the turbulent eddies (otherwise the eigenvalues and eigenfunctions would not differ from one type of turbulence to another). Extracting this information is not, in general, as simple as examining the structure of the individual eigenfunctions, since it is well known that the eigenfunctions of any form of homogeneous turbulence are trigonometric functions, and eddies are not waves.

In an early approach to this problem, Lumley (1970) coupled POD analysis with the assumption that the flow could be represented as a shot noise process to extract structures called the characteristic eddies. Bakewell & Lumley (1967) obtained the most energetic eddy structure in the wall region, $y^+ < 40$, in a turbulent pipe flow at $Re_D = 8700$. (Re_D is the Reynolds number based on bulk velocity and pipe diameter, and $y^+ = yu_\tau/v$ is the inner layer coordinate made non-dimensional by the viscous length scale based on the friction velocity u_τ and the kinematic viscosity v.) They measured only the $Re_{11}(r_x)$ component of the correlation tensor, and obtained the other components by using a mixing-length assumption and conservation of mass. One eigenmode was calculated. The assumption of zero phase was used to reconstruct a typical eddy, which carried over 90% of the total streamwise turbulent intensity. They concluded that the dominant structure in the buffer layer consists of counter-rotating eddy pairs of elongated extent that are tilted in the upstream direction.

Herzog (1986) measured four components of the correlation tensor $R_{ij}, i,j = 1,3$, at six points in the wall-normal and circumferential directions and at seven points in the streamwise direction in a pipe flow at $Re_D = 8750$ ($u_\tau R/v = 265$, where R is the pipe radius). The rest of the components of the tensor were reconstructed from continuity. The decomposition domain, $0 \leqslant y^+ \leqslant 40$, was far too small to encompass the large-scale structures we are interested in here, but the results they found for the buffer-layer structure are of interest for later comparison. The maximum eigenvalue was found to be dominant for a wavenumber of $k_1v/u_\tau = 0$, $n = 1$ and $k_3v/u_\tau = 0.0035$. The first eigenmode contained 60% of the streamwise turbulent intensity, and the first three eigenmodes contained almost all of the total energy. A shot noise expansion was used to determine the phase of a typical eddy. With a zero-phase reconstruction, a typical eddy was found to be a pair of counter-rotating vortices whose centres were 30–$40v/u_\tau$ above the wall, $65v/u_\tau$ apart, and $400v/u_\tau$ in extent. They were tilted at $5°$ to the wall.

Moin & Moser (1989) applied POD to one (y), two $(y$-$z)$ and three-dimensional

decompositions of turbulent channel flow at low Reynolds number ($Re_h = U_b h/v = 2800$, where U_b is the bulk velocity, and h is the half-height of the channel; $Re_\tau = u_\tau h/v = 180$). The two-point velocity correlation tensor $R_{ij}(r_x, y, y', r_z), i, j = 1, 2, 3$, was computed using the DNS data on three different domains: $0 < y^+ < 40$, $140 < y^+ < 180$ and $0 < y^+ < 180$. A shot noise expansion was used to determine the phase. The resulting zero-phase characteristic eddy, which contributed as much as 76% of the kinetic energy, was found to consist of a narrow ejection straddled by a pair of weak, streamwise, counter-rotating vortices with a streamwise extent of less than 100^+. They were inclined at $10°$ near the wall, and as much as $60°$ farther away from the wall. Sirovich *et al.* (1990, 1991) also used DNS data to calculate correlation and spectral tensors at low Reynolds numbers ($u_b h/v = 1200, 1800; u_\tau h/v = 80, 125$). They considered only the $Re_h = 1800$ study to be fully developed. The decomposition domain was the full channel height. A three-dimensional decomposition was performed; 16 modes with wavenumbers ($k_1 = 0$–1, $n = 1$–2, $k_3 = 0$–3) were found to account for 60% of the total energy in the flow, where k_1 and k_3 denote the numbers of full waves in the streamwise and spanwise directions and n is the eigenmode order in the wall-normal direction. The most energetic mode with $k_1 \neq 0$ for the two cases is $k_1 = 1$, $n = 1$, $k_3 = 3$.

All of the foregoing POD results pertain to low-Reynolds-number channel flow. The behaviour at high Reynolds number is less well understood. Chambers *et al.* (1988) used Burgers' equation with random forcing to create a stationary, spatially inhomogeneous flow structure possessing the characteristics of a two-scale boundary layer at the endpoints of the unit interval. The POD eigenfunctions in the inhomogeneous spatial variable were found to be similar, over a range of Reynolds numbers, when they were scaled with outer variables. They suggested that the POD of real turbulence might also obey such a generalized law of Reynolds number similarity.

Liu, Adrian & Hanratty (1994, 1995) obtained the POD from measurements in the (x, y)-plane of channel flow at the same Reynolds numbers as reported here. The structure of the one-dimensional POD eigenfunctions consisted of a thin layer close to the wall, of order of the buffer-layer thickness, in which the modes decreased rapidly to zero at the wall, and an outer region in which the structure of the modes was essentially independent of the Reynolds number. The eigenvalue spectra of the channel flow were shown to correlate well with those of a boundary-layer flow (Lu & Smith 1991), supporting the notion that outer-layer similarity applies to at least two types of wall turbulence. Outer-layer Reynolds similarity of the POD is a stronger form of similarity than that found from the mean velocity. Its validity is based on data at a relatively low Reynolds number; so further work is needed to test its generality for all Reynolds numbers. Even so, outer similarity of the POD modes suggests that the form of the large-scale motions and the amounts they contribute to energy and Reynolds stress may also be independent of Reynolds number.

This paper examines the significance and structure of large-scale motions of turbulent flow in a channel. Particle image velocimetry (Adrian 1991) is used to capture, at different instances of time, the spatial variation of the two components of the velocity in a plane that is perpendicular to the wall and oriented in the flow direction (*x*-*y*). Two-dimensional spatial correlations are determined by averaging many realizations of the flow. These correlations are analysed by proper orthogonal decomposition to arrive at a representation of the flow field as the sum of 5346 two-dimensional orthogonal eigenfunctions.

Two Reynolds numbers were studied $Re_h = U_b h/v = 5378$ and $29\,935$ (or $Re_\tau = u_\tau h/v = 315$ and 1414, where U_b is the bulk velocity, and h is the half-height of the

channel). These conditions are identical to those in Liu *et al.* (1991, 1994). Because of limitations in the spatial resolution of PIV close to the wall, all of these studies focus on the outer flow, for which the appropriate length scale is normally assumed to be independent of Reynolds number and proportional to the channel height.

By virtue of the orthogonality property, the contributions of each POD mode to the total Reynolds stress and to the total energy are additive. In this way, it is shown that most of the Reynolds stress is carried by a small number of eigenmodes representing large-scale events. Each instantaneous measurement of the velocity field can be represented by a linear combination of the eigenfunctions. By summing the small number of eigenfunctions that contain most of the Reynolds stress, the coherent structure of interest, in an individual realization of the field, can be captured. Since these are the large-scale motions, this procedure represents a low-pass filtration. Similarity is explored by comparing, at the two Reynolds numbers, the two-dimensional spatial correlations and the fractional contributions of the different eigenmodes to the Reynolds stress and to the kinetic energy.

The research described in this paper and in Liu *et al.* (1994, 1995) differs from previous POD studies in that it uses laboratory measurements at a much larger number of points, and it studies larger Reynolds numbers. The interpretation of the eigenfunctions is also somewhat different from previous studies in that no attempt is made to use the eigenfunctions to represent a characteristic eddy. Instead, the structure of the large eddies is found by using the eigenfunctions as a low-pass filter that extracts the motions that are large contributors to the Reynolds stress (Liu *et al.* 1995).

2. Experimental procedures

Physical lengths made dimensionless by the viscous length scale are denoted by the usual notation (x^+, y^+, z^+), but fluctuating velocity components normalized by the wall-friction velocity u_τ are denoted by $(u, v, w) = (u_1, u_2, u_3)$, the superscript '+' being omitted to avoid clutter in the POD equations. The two-dimensional channel flow facility contained water, and its rectangular cross-section was 609.6 mm wide by $2h = 48.75$ mm high. The channel and the single-lens photographic particle image velocimeter used to measure velocity in this study have been described in studies by Niederschulte, Adrian & Hanratty (1990), Warholic (1997) and Guenther *et al.* (1998). All of the experimental measurements of conventional turbulence statistics through fourth-order are consistent with generally accepted behaviour of channel flow, as found in the experiments of other investigators, and in direct numerical simulations.

The PIV provided instantaneous measurements of (u, v) on an (x, y)-plane that extended from $y = 0$, to $y = 2h$, and the length of the data domain in the streamwise direction was $L_x = 78$ mm $= 3.2h$, as determined by the field-of-view of the PIV camera. More than 5000 vectors were calculated from each PIV photograph, and an ensemble of 60–80 photographs was obtained at each Reynolds number. The flow parameters are given in table 1. The measurement volume used to obtain a vector during interrogation was $(\Delta x_0, \Delta y_0, \Delta z_0) = (1.6 \text{ mm}, 0.8 \text{ mm}, 0.8 \text{ mm})$. These dimensions normalized with viscous wall units and with the outer length scale, h, are given in table 2. The spacing between vectors was 1.2 mm in the x-direction and 0.6 mm in the y-direction. The measurements closest to the wall were at $y^+ = 5.16$ and 23.2^+ for the two Reynolds numbers. At the lower Reynolds number, the spatial resolution is comparable to that achieved in direct numerical simulations, but at the higher Reynolds number, each measured vector represents an average over a significant

$U_b h/v$	$u_\tau h/v = h^+$	L_x^+	U_b (mm s^{-1})	u_τ (mm s^{-1})	v/u_τ (mm)
5378	315	1008	212	12.4	0.0775
29 935	1414	4520	1074	50.7	0.0172

TABLE 1. Flow parameters.

$U_b h/v$	Δx_0^+	Δy_0^+	Δz_0^+	$\Delta x_0/h$	$\Delta y_0/h$	$\Delta z_0/h$
5378	20.6	10.3	10.3	0.065	0.032	0.032
29 935	93.0	46.5	46.5	0.065	0.032	0.032

TABLE 2. The measurement volume in the PIV experiments.

range of small scales. For example, the resolution in the y-direction $\Delta y_0^+ = 46.5$ was clearly inadequate to resolve the buffer layer. However, its size relative to the outer scale, $\Delta y/h = 0.032$, was small enough to allow the evaluation of 15 POD modes in the y-direction. Thus, the range of validity of our measurements of the POD modes and eigenvalue spectra is restricted to the lower orders that are adequately resolved by the measurements.

3. Proper orthogonal decomposition

Proper orthogonal decomposition of the experimental channel flow data is performed on the domain $(0 \leqslant x/L_x \leqslant 1, 0 \leqslant y/2h \leqslant 1)$, where the streamwise coordinate x is normalized by $L_x = 3.2h$, and the wall-normal coordinate y is normalized by $2h$. Since the flow is fully developed, its statistics are homogeneous in the streamwise direction, and the eigenfunctions of the POD are trigonometric in x. Therefore, on $(0 \leqslant x/L_x \leqslant 1, 0 \leqslant y/2h \leqslant 1)$ we can represent the ith component of the velocity, $u_i(x, y)$ by the Fourier series

$$u_i(x, y) = \sum_k \hat{u}_i(k, y) \exp(j2\pi kx/L_x), \tag{1}$$

where the Fourier coefficient

$$\hat{u}_i(k, y) = \frac{1}{L_x} \int_0^{L_x} u_i(x, y) \exp(-j2\pi kx/L_x) \, dx, \tag{2}$$

is a random function of the inhomogeneous direction y with parameter k. (Note that the wavenumber k in (2) is defined so as to be an integer, rather than 2π over a wavelength.) The two-dimensional proper orthogonal decomposition is completed by expanding $\hat{u}_i(k, y)$ in a Karhunen–Loève expansion

$$\hat{u}_i(k, y) = \sum_n a^{(k,n)} \phi_i^{(k,n)}(y), \tag{3}$$

wherein the basis functions $\phi_i^{(k,n)}(y)$ are orthogonal,

$$\frac{1}{2h} \int_0^{2h} \phi_i^{(k,n)}(y) \phi_i^{(k,n')^*}(y) \, dy = \delta_{nn'}. \tag{4}$$

The Fourier coefficients are given by

$$a^{(k,n)} = \frac{1}{2h} \int_0^{2h} \phi_i^{(k,n)^*}(y) \hat{u}_i(k,y) \, \mathrm{d}y. \tag{5}$$

Requiring the Fourier coefficients to be statistically orthogonal,

$$\langle a^{(k,n)} a^{(k',n')^*} \rangle = \lambda^{(k,n)} \delta_{nn'} \, \delta_{kk'}, \tag{6}$$

and requiring the basis functions $\phi_i^{(k,n)}(y)$ to have the property that the partial sums of (3) converge faster than the partial sums of any other set of orthogonal functions results in the following integral equation for $\phi_i^{(k,n)}(y)$:

$$\frac{1}{2h} \int_0^{2h} K_{ij}^{(k)}(y,y') \phi_j^{(k,n)}(y') \, \mathrm{d}y' = \lambda^{(k,n)} \phi_i^{(k,n)}(y) \quad (i,j = 1,2), \tag{7}$$

where

$$K_{ij}^{(k)}(y,y') = \langle \hat{u}_i(k,y) \hat{u}_i^*(k,y') \rangle. \tag{8}$$

The kernel $K_{ij}^{(k)}(y,y')$ is related to the two-point spatial correlation tensor

$$R_{ij}(r_x, y, y') = \langle u_i(x,y) u_j^*(x + r_x, y') \rangle, \tag{9}$$

by

$$K_{ij}^{(k)}(y,y') = \frac{1}{L_x} \int_0^{L_x} (1 - r_x/L_x) R_{ij}(r_x, y, y') \exp(j2\pi k r_x/L_x) \, \mathrm{d}r_x. \tag{10}$$

The spatial correlation tensor is calculated from the PIV data by forming the product of velocity components, ensemble averaging over the ensemble of experimental fields, and line averaging over the x-direction. The ensemble average for a given (r_x, y, y') extends only over those realizations that have valid vector data at those points. The effect of missing data is accounted for by dividing by the number of valid data in the ensemble at each point. The separations between the two points in the correlation functions are in the wall-normal and streamwise directions. Separations in spanwise direction and time-lags are not considered.

Combining the foregoing equations gives

$$u_i(x,y) = \sum_k \sum_n a^{(k,n)} \psi_i^{(k,n)}(x,y), \tag{11}$$

where

$$\psi_i^{(k,n)}(x,y) = \phi_i^{(k,n)}(y) \exp(j2\pi k x/L_x) \tag{12}$$

is the two-dimensional orthogonal eigenfunction of the complete POD expansion. It satisfies the orthogonality condition,

$$\frac{1}{2hL_x} \int_0^{2h} \int_0^{L_x} \psi_i^{(k,n)}(x,y) \psi_i^{(k',n')^*}(x,y) \, \mathrm{d}x \mathrm{d}y = \delta_{nn'} \delta_{kk'}. \tag{13}$$

The eigenfunction of the ith velocity component $\phi_i^{(k,n)}(y)$ is a Fourier mode of order k in the streamwise direction and order n in the wall-normal direction. The order k is associated with a wavelength L_x/k, i.e. k equals the number of sinusoidal wavelengths in the domain L_x. It is related to the streamwise wavenumber by $k_x = (2\pi/L_x)k$. The principal usefulness of the POD is that it also associates a length scale in the y-direction with the modal order n. However, since the statistical inhomogeneity in this direction implies varying length scale, the modal order n cannot be related to a

single length. Rather, the structure of the eigenfunction itself defines a range of length scales for each mode. It has been shown that the modes approach trigonometric form as the modal order increases (Moser 1994; Sung & Adrian 1994), so the mode becomes associated with a length scale $2h/n$ for large n. Thus, POD decomposition makes it possible to evaluate the contribution of structures on the basis of their size in both the streamwise and the wall-normal directions, i.e. structures that are, for example, long in x, but narrow in y, or structures that are large in both x and y.

The contributions of structures of various sizes can be evaluated quantitatively by summing the contributions from the various modes. This is possible because the modes are statistically uncorrelated. For the turbulent kinetic energy,

$$E = \frac{1}{2h} \int_0^{2h} \langle u_i(x, y) u_i^*(x, y) \rangle \, dy = \sum_k \sum_n \lambda^{(k,n)}. \tag{14}$$

For the turbulent Reynolds stress,

$$\langle u_i(x, y) u_j^*(x, y) \rangle = \sum_k \sum_n \lambda^{(k,n)} \phi_i^{(k,n)}(y) \phi_j^{(k,n)^*}(y), \tag{15}$$

and

$$\frac{1}{2h} \int_0^{2h} \langle u_i(x, y) u_j^*(x, y) \rangle \, dy = \sum_k \sum_n \lambda^{(k,n)} \frac{1}{2h} \int_0^{2h} \phi_i^{(k,n)}(y) \phi_j^{(k,n)^*}(y) \, dy. \tag{16}$$

Superscript n represents the mode order in the inhomogeneous wall-normal direction. In a one-dimensional decomposition (Liu *et al.* 1994) n equals the number of zero-crossings of the eigenfunction. However, in two- or three-dimensional decomposition, the interpretation is more complicated, because the eigenfunctions are complex. $\lambda^{(k,n)}$ is the eigenvalue of the mode with orders n and k.

4. Distribution and structure of energy and transport

4.1. *The two-point correlation functions*

Contours of the two-point correlation coefficients with separations in both y- and x-directions, $R_{ij}(r_x, y, y')/\sigma_i(y)\sigma_j(y'), i, j = u, v$, are plotted in figure 1 for $Re_h = 5378$ and in figure 2 for $Re_h = 29\,935$. Here, σ_i denotes the root-mean-square value of the fluctuation of the ith-component of velocity. The correlation functions are given for the fixed point, y, located at four different distances from the wall: $y/h = 0.065$, 0.237, 0.508 and 1.0. These correspond to $y^+ = 20.5$, 75, 160 and 315 for the lower Reynolds number, and $y^+ = 92$, 335, 718 and 1414 for the higher Reynolds number. Statistical sampling error of the two-dimensional correlation functions is estimated to be less than $\pm 10\%$ of the peak correlation value.

In the outer region the correlation contours for the two Reynolds numbers are qualitatively similar when the separations of the two points in both the x- and y-directions are scaled with h, partially supporting the notion that the structure of large-scale motions exhibits Reynolds number similarity (Townsend 1976). However,

FIGURE 1. Contours of the two-point correlation coefficients for $Re_h = 5378$. (a)(i)–(a)(iv), $R_{uu}(r_x, y, y')/\sigma_u(y)\sigma_u(y')$; (b)(i)–(b)(iv), $R_{vv}(r_x, y, y')/\sigma_v(y)\sigma_v(y')$; (c)(i)–(c)(iv), $R_{uv}(r_x, y, y')/\sigma_u(y)\sigma_v(y')$; (d)(i)–(d)(iv), $R_{vu}(r_x, y, y')/\sigma_v(y)\sigma_u(y')$. The locations of the fixed correlating points are: (a)(i)–(d)(i), $y/h = 0.065$ $(y^+ = 20.5)$; (a)(ii)–(d)(ii), $y/h = 0.237$ $(y^+ = 75)$; (a)(iii)–(d)(iii), $y/h = 0.508$ $(y^+ = 160)$; (a)(iv)–(d)(iv), $y/h = 1.0$ $(y^+ = 315)$.
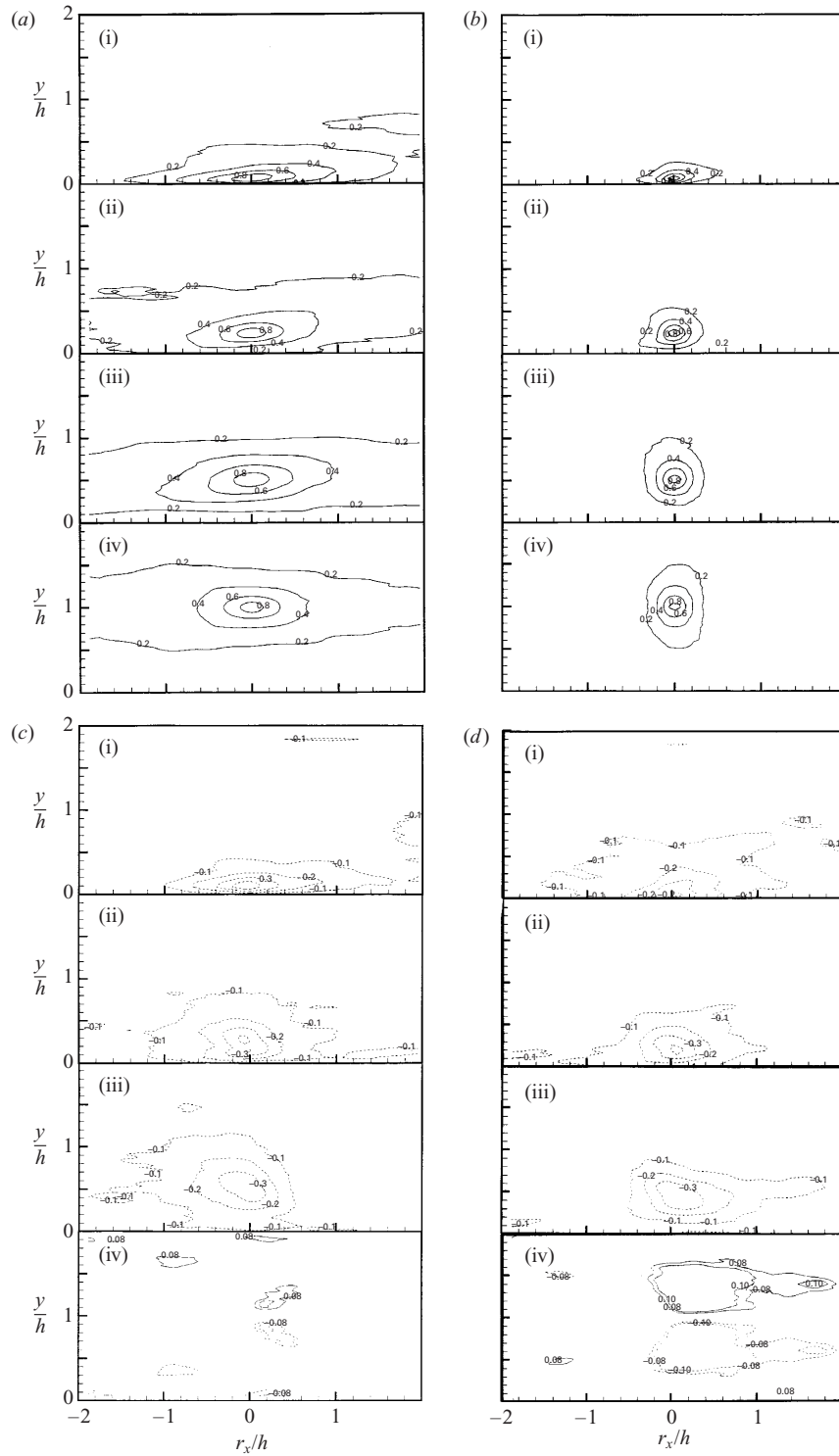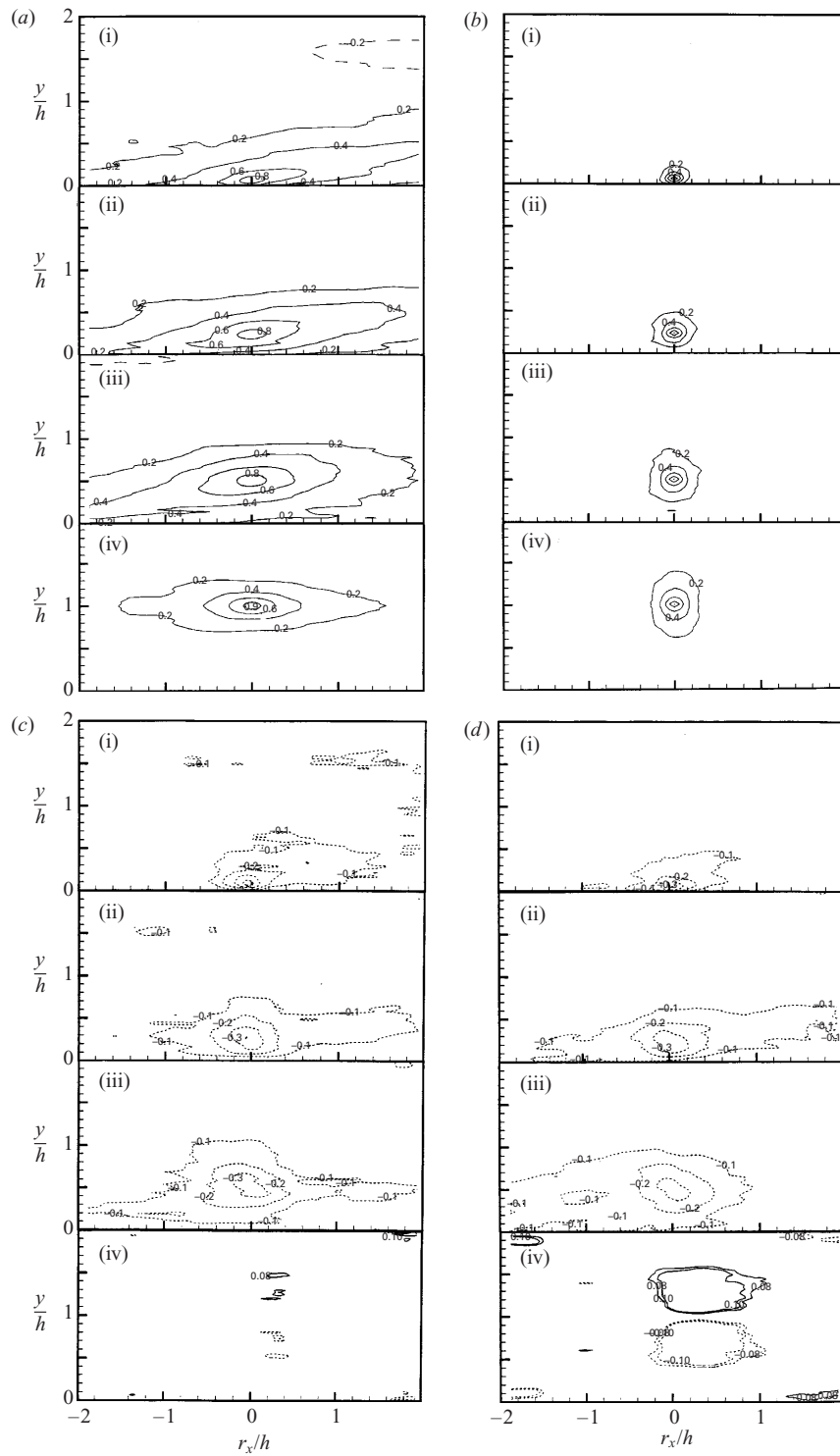
FIGURE 1. For caption see facing page.

FIGURE 2. For caption see facing page.

there are some differences, one being a tendency for the highly correlated regions (~ 0.8 or higher) of the higher-Reynolds-number data to be smaller than the highly correlated region of the lower-Reynolds-number data. This effect is expected because the ratio between the Taylor microscale and the integral length scale decreases with increasing Reynolds number. A more fundamental Reynolds-number effect that is definitely concerned with the larger scales can be seen in the streamwise extent of the streamwise velocity correlation. Relative to the lower-Reynolds-number case, the length of the correlated region at the higher Reynolds number is longer close to the wall (compare figures 2ai and 2$a$ii to figures 1ai and 1$a$ii) and shorter farther away from the wall (compare figures 2$a$iii and 2$a$iv to figures 1$a$iii and 1$a$iv). In Adrian *et al.* (2000) it is argued that the streamwise extent of the streamwise velocity autocorrelation reflects the organization of near-wall eddies into packets and the resulting correlation of the u-fluctuations induced by successive eddies. The length of a packet increases with increasing Reynolds number because there are more eddies per packet.

Autocorrelations of the streamwise component for fixed points not on the centreline exhibit a characteristic shape that is elongated in the streamwise direction and inclined at a shallow angle to the wall. The average angle is $6°$ and $8°$ at the lower and higher Reynolds numbers, respectively. Symmetry forces the inclination to vanish when the fixed point is at the centreline of the channel. The length and height of the region of high positive correlation grow with increasing distance of the fixed point from the wall. The streamwise length attains a value in excess of $4h$, cf. figures 1(a)(iii), 2(a)(ii) and 2(a)(iii). Autocorrelations of the v-component also grow as the fixed point moves away from the wall. This is consistent with Townsend's (1976) attached-eddy hypothesis which states, in part, that eddies extend down to the wall such that eddies centred at y have wall-normal scale of order y. However, the v-correlations have roughly circular contours, in sharp contrast to the elongated contours of the u-component autocorrelation.

The v-correlations are also short relative to the u-correlations. For example, for the fixed point at $y/h = 0.237$, the length of the region in which the u-correlation coefficient exceeds 40% is $1.5h$ (126 viscous wall units) in figure 1(a)(ii) while the corresponding length of the v-correlation coefficient in figure 1(b)(ii) is only $0.4h$, a ratio of almost $4:1$. At the higher Reynolds number, the length of the u-correlation is $3.4h$ compared to $0.3h$ (424 viscous wall units) for the v-correlation, a ratio of more than $10:1$. Although the extent of the v-correlations, of order 0.3–$0.4h$ is relatively small, the motions associated with the v-component are still large scale, in the sense that they scale with h. Inspection of the u–v cross-correlations reveals that they are elongated, much like the u-correlations (although somewhat shorter). This suggests that the largest-scale motions contain a significant fraction of the Reynolds shear stress and only a small fraction of the v-component energy. To evaluate the exact amounts, we must perform proper orthogonal decomposition.

The two-point cross-correlation coefficients for u–v and v–u are shown in figures 1 and 2 for completeness. Their length scales are intermediate to those of the u–u and the v–v autocorrelations. Cross-correlation coefficients have negative values around

FIGURE 2. Contours of the two-point correlation coefficients for $Re_h = 29\,935$. (a)(i)–(a)(iv), $R_{uu}(r_x, y, y')/\sigma_u(y)\sigma_u(y')$; ($b$)(i)–($b$)(iv), $R_{vv}(r_x, y, y')/\sigma_v(y)\sigma_v(y')$; ($c$)(i)–($c$)(iv), $R_{uv}(r_x, y, y')/\sigma_u(y)\sigma_v(y')$; ($d$)(i)–($d$)(iv), $R_{vu}(r_x, y, y')/\sigma_v(y)\sigma_u(y')$. The locations of the fixed correlating points are: (a)(i)–(d)(i), $y/h = 0.065$ ($y^+ = 92$); (a)(ii)–(d)(ii), $y/h = 0.237$ ($y^+ = 335$); (a)(iii)–(d)(iii), $y/h = 0.508$ ($y^+ = 718$); (a)(iv)–(d)(iv), $y/h = 1.0$ ($y^+ = 1414$).

the fixed point, and with zero separation, the coefficients are approximately -0.41 over most of the channel. When the fixed point is on the centreline of the channel, the cross-correlation coefficients are anti-symmetric with respect to y. When the fixed point is off the centreline, the anti-symmetry persists to the extent that the correlation coefficients tend to have opposite signs above and below the centreline. Thus, second quadrant events in the lower half of the channel which produce strong negative values of the uv-product, tend to be associated with positive uv-events in the upper half of the channel. Note that the latter is equivalent to a second quadrant event since the normal to the upper wall is in the downward direction.

4.2. *Eigenfunctions and eigenvalue spectra*

Equation (7) was solved for the eigenfunctions and eigenvalues for each k using trapezoidal quadrature and an IMSL eigenproblem subroutine. The number of eigen-modes in the decomposition was 5346, with 33 modes ($k = 0$–32) in the streamwise homogeneous direction and 162 modes ($n = 1$–162) in the wall-normal direction.

The eigenfunctions for the two Reynolds numbers with the domain of $2h$ are plotted in figure 3 for $k = 0$ and 1 and $n = 1, 2, 3$ and 4. The non-dimensional eigenfunctions of the two-dimensional decomposition are $(hL_x)^{1/2}\phi_i^{(k,n)}(y)$ and the non-dimensional eigenvalues are $\lambda^{(k,n)}/(u_\tau^2 hL_x)$. The factor of $(hL_x)^{1/2}$ is determined by the orthogonality of eigenfunctions (13), and the factor $(u_\tau^2 hL_x)$ comes from equation (7). The imaginary parts of all $k = 0$ eigenmodes are zero, but for $k > 0$ the eigenfunctions are complex. The figures show only the real parts. Both real and imaginary parts of eigenfunctions contribute to the energy and Reynolds stress associated with each eigenmode. The phases between eigenfunctions of the u- and v-components do not influence the contributions of the eigenmodes to the turbulent kinetic energy. However, they are very important in determining the contributions of the eigenmodes to the Reynolds shear stress, as can be seen from equation (15). The phases are mostly opposite in sign in the lower half of the channel and have the same sign in the upper half of the channel. This results in positive contributions to the Reynolds stress in both halves of the channel.

The eigenfunctions for both components are alternately symmetric and anti-symmetric about the centre of the channel for successive orders of the wall-normal modes and streamwise modes. For each eigenmode, the symmetries of the eigenfunc-tions for the two components are always opposite. As a consequence, contributions of each of the eigenmodes to the Reynolds stress are mostly positive. There is a simple rule which can be used to identify the symmetry of the eigenfunctions in terms of eigenmode orders k and n. If $(k+n)$ is odd, the eigenfunctions for the u-component are symmetric and the eigenfunctions of the v-component are anti-symmetric. If $(k+n)$ is even, the opposite is true. This feature of the eigenfunctions reveals that contributions to the Reynolds stress are statistically positive, and that both the upper and the lower halves of the channel are statistically identical.

Equations (14)–(16) can be used to evaluate the contributions of the different eigenmodes, and hence different scales of eddies, to the energy and the Reynolds stress. Each mode makes its contribution independently because of the orthogonality of the eigenfunctions. The $k = 0$ modes require careful interpretation. From equations (2) and (3) the $k = 0$ modes are given by

$$\hat{u}_i(0, y) = \frac{1}{L_x} \int_0^{L_x} u_i(x, y)\, \mathrm{d}x = \sum_n a^{(0,n)}\phi_i^{(0,n)}(y). \tag{17}$$

| Order | (k, n) | Fractional energy (%) | | D |
		$Re_h = 5378$	$Re_h = 29\,935$	
1	$(0, 1)$	10.5	13.8	1
2	$(0, 2)$	8.92	9.08	1
3	$(1, 1)$	5.28	5.81	2
4	$(1, 2)$	4.92	4.87	2
5	$(1, 3)$	3.54	3.28	2
6	$(0, 3)$	2.86	2.58	1
7	$(0, 4)$	2.64	1.93	1
8	$(2, 1)$	2.39	2.03	2
9	$(1, 4)$	2.36	2.24	2
10	$(2, 2)$	1.72	1.84	2
11	$(1, 5)$	1.61	1.15	2
12	$(0, 5)$	1.41	1.25	1
13	$(2, 3)$	1.29	1.3	2
14	$(1, 6)$	1.21	1.12	2
15	$(2, 4)$	1.17	0.94	2
16	$(0, 6)$	1.15	0.50	1
17	$(3, 1)$	1.1	1.0	2
18	$(1, 7)$	0.95	0.60	2
19	$(3, 2)$	0.91	1.0	2
20	$(3, 3)$	0.91	0.69	2
6 modes	$(0\text{–}2, 1\text{–}2)$	33	37	
12 modes	$(0\text{–}2, 1\text{–}4)$	48	50	

TABLE 3. Fractional contributions of the two-dimensional eigenmodes to the total turbulent kinetic energy for $Re_h = 5378$ and $29\,935$. The eigenmode indices are denoted by (k, n). The table is arranged in descending order of the energy contributions at low Reynolds number, $Re_h = 5378$. D is the degeneracy of the eigenmode in the streamwise direction.

Thus, the $(0, n)$ eigenfunctions represent decomposition of the line average of the fluctuating velocity over the streamwise length of the domain, L_x. If L_x were infinite, ergodicity of line averages in the homogeneous streamwise direction would imply that the line average of each fluctuating velocity component is zero, and hence all $(0, n)$ modes would vanish. When L_x is finite, the integral in (17) can be interpreted as a running average, which acts as a low-pass filter. All modes of wavelength L_x or less integrate to zero, so the $k = 0$ modes represent the contribution from all motions whose wavelengths are longer than L_x.

Table 3 gives the fractional contribution of each eigenmode of order (k, n) to the total energy. They are energy-ordered for the $Re_h = 5378$ modes. Table 4 gives the fractional contribution of each eigenmode to the total Reynolds shear stress as calculated from equation (16) by integrating the eigenfunction products across the channel. The contributions are arranged in descending order of the $Re_h = 5378$ modes (the descending ordering is slightly different for the higher Reynolds number). Both of these quantities represent contributions to the total value integrated across the channel. The $(0, 1)$ modes for $Re_h = 5378$ and $29\,935$ contain 10.5% and 13.8% of total energy, respectively, and they are the strongest contributors to the energy. The largest contributors to the total Reynolds stress are the $(0, 2)$ modes, which contain 13.3% and 13.6% of total Reynolds stress for $Re_h = 5378$ and $Re_h = 29\,935$. The first six modes $(k = 0\text{–}2, n = 1\text{–}2)$ out of a total of 5346 eigenmodes contribute more than a third of the total energy and half of the total Reynolds stress for both Reynolds numbers. The

Order	(k, n)	Fractional Reynolds stress (%)		D
		$Re_h = 5378$	$Re_h = 29\,935$	
1	$(0, 2)$	13.3	13.6	1
2	$(1, 1)$	12.28	9.2	2
3	$(0, 1)$	10.81	7.81	1
4	$(1, 2)$	9.16	10.2	2
5	$(2, 1)$	6.25	5.56	2
6	$(1, 3)$	4.92	0.24	2
7	$(2, 2)$	4.3	3.95	2
8	$(1, 4)$	3.8	3.77	2
9	$(2, 4)$	3.03	1.72	2
10	$(0, 4)$	2.88	2.4	1
11	$(3, 1)$	2.69	2.76	2
12	$(0, 3)$	2.5	1.26	1
13	$(3, 3)$	2.29	1.36	2
14	$(3, 2)$	2.22	3.95	2
15	$(2, 3)$	2.02	2.11	2
16	$(4, 1)$	1.73	1.57	1
17	$(1, 6)$	1.71	1.28	2
18	$(4, 2)$	1.3	1.28	2
19	$(3, 4)$	1.28	0.186	2
20	$(1, 5)$	0.734	0.254	2
6 modes	$(0\text{–}2, 1\text{–}2)$	56	50	
12 modes	$(0\text{–}2, 1\text{–}4)$	75	67	

TABLE 4. Fractional contributions of the two-dimensional eigenmodes to the total Reynolds stress for $Re_h = 5378$ and $29\,935$. The eigenmode indices are denoted by (k, n). The table is arranged in descending order of the Reynolds stress contributions at low Reynolds number, $Re_h = 5378$. D is the degeneracy of the eigenmode in the streamwise direction only.

first 12 eigenmodes ($k = 0\text{–}2, n = 1\text{–}4$) contain almost half of the total energy and two-thirds to three-quarters of the total Reynolds stress. These modes consist of structures whose lengths in the streamwise direction are $\frac{1}{2}L_x = 1.6h$ ($k = 2$), $L_x = 3.2h$ ($k = 1$), and all modes longer than L_x ($k = 0$). In the y-direction, the length scales associated with the modes $n = 1\text{–}4$ range from $2h$ down to $0.3h$ (cf. figure 3), which are still large, considering that the thickness of the logarithmic layer is no more than $0.2h$.

These results compare well with direct numerical simulations of channel flow at low Reynolds numbers. Sirovich *et al.* (1990) give the eigenvalue spectrum for three-dimensional decomposition of a very low (barely transitional) Reynolds number ($Re_h = 1500, Re_\tau = 80$). Summing over the first four modes in the spanwise direction gives an approximate two-dimensional decomposition that can be compared to the present results. The first six most energetic modes are identical to those found in table 3, but they contain rather more energy, 67% versus 33% at $Re_h = 5378$. At approximately twice the Reynolds number ($Re_h = 2800, Re_\tau = 180$) one-dimensional POD on the half-channel domain ($0 < y^+ < 180$) gives 32% of the total kinetic energy and 66% of the Reynolds stress in just the first three modes (Moin & Moser 1989). The dominance of the lower-order modes in the direct numerical simulations is not surprising, because the spectrum of the turbulence has a fairly small range of scales at low Reynolds numbers. However, the relatively similar behaviour of the present results at substantially higher Reynolds numbers indicates that dominance of the large-scale modes persists, even as the spectrum widens.
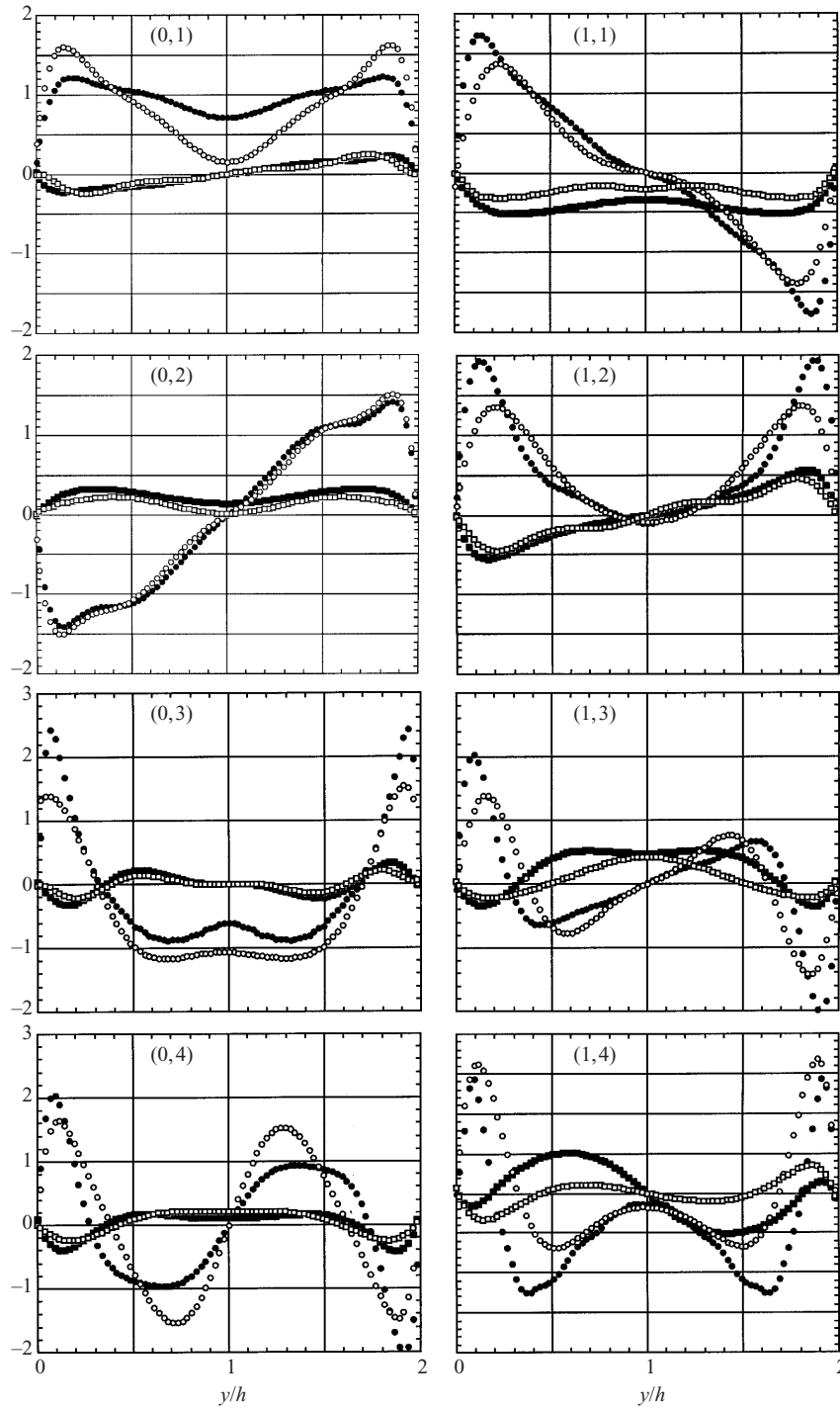
FIGURE 3. The real part of the two-dimensional eigenfunctions for various mode orders (k, n). ○, $(hL_x)^{1/2}\phi_u^{(k,n)}(y)$; □, $(hL_x)^{1/2}\phi_v^{(k,n)}(y)$. Solid symbols represent $Re_h = 5378$, and open symbols represent $Re_h = 29\,935$.
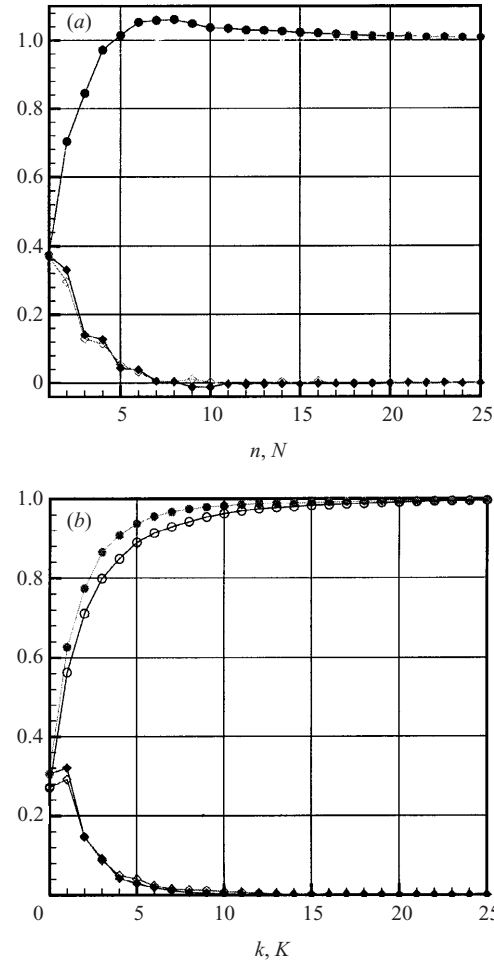
FIGURE 4. Fractional Reynolds stress contributions. (*a*) diamonds, $\sum_{all\,k}\langle uv\rangle^{(k,n)}$; circles, cumulative Reynolds stress of the first N wall-normal eigenmodes, $\sum_{all\,k}\sum_{n=1-N}\langle uv\rangle^{(k,n)}$; (*b*) diamonds, $\sum_{all\,n}\langle uv\rangle^{(k,n)}$; circles, cumulative Reynolds stress of the first K streamwise eigenmodes, $\sum_{all\,n}\sum_{k=0-K}\langle uv\rangle^{(k,n)}$. Solid symbols, $Re_h = 5378$; open symbols, $Re_h = 29\,935$.

The fact that the largest-scale motions in the streamwise and the wall-normal directions are the most important contributors to the turbulent kinetic energy is consistent with the early observations of Grant (1958) and Townsend (1958) and subsequent investigations, which were also at moderate Reynolds numbers. The fact that these scales also carry more than two-thirds of the total Reynolds shear stress is quite surprising, and completely at odds with the notion that the large scales are not important to the transport of momentum and hence 'inactive' (Townsend 1976). Even the first 6 modes that contain 33–37% of the kinetic energy contain 50–56% of the Reynolds shear stress. The inescapable conclusion is that large-scale motions play a very important role in the transport of momentum, at least for the range of Reynolds numbers considered here.

What about the small-scale motions, especially those in the near-wall buffer layer where they are most active? The contribution of higher-order modes to the total Reynolds shear stresses is shown graphically in figure 4. For the lower modes shown
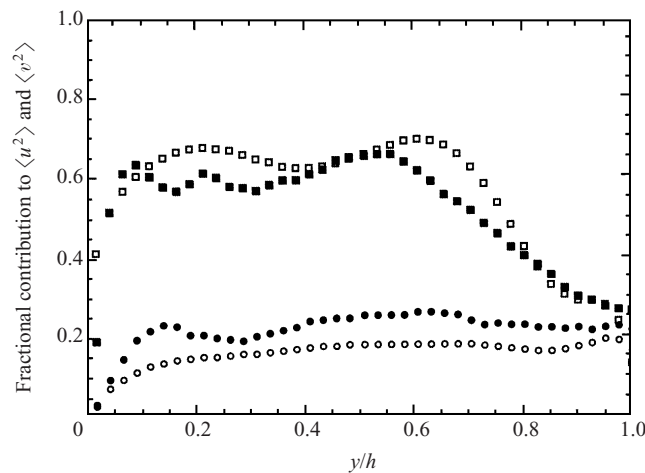
FIGURE 5. Profiles of the fractional contributions of the first 12 eigenmodes ($k = 0$–$2, n = 1$–4) to □, the kinetic energies of streamwise, and ○, the wall-normal velocities. Solid symbols, $Re_h = 5378$; open symbols, $Re_h = 29\,935$.

in table 4, the modes all contribute positively, but, in general, the contribution of a single mode to the Reynolds stress can be positive or negative. Figure 4(a) gives the spectrum of total contributions to the Reynolds stress of modes, n, summed over all wavenumbers, k, and the cumulative contributions of all modes with $n \leqslant N$. The lower-order modes for $Re_h = 5378$ actually overshoot the total mean value up to $n = 8$, after which slightly negative values return the total to 100% of the total contribution. A similar phenomenon was reported by Moin & Moser (1989). The overshoot is minor at the higher Reynolds number. For both cases, 10 modes in n and all the modes in k suffice to carry all of the Reynolds shear stress. Figure 4(b) gives the total contribution to the Reynolds stress for different Fourier modes, k, summed over all Karhunen–Loeve modes, n, and the cumulative contributions for $k \leqslant K$.

As indicated earlier, the contributions inferred from the eigenvalues refer to the total values of the kinetic energy and the Reynolds stress integrated across the channel. It is possible for the large-scale motions to dominate the integrated value while the small-scales dominate locally in a region such as the buffer layer. Figure 5 presents the local fractional contributions to the total energy of the streamwise and wall-normal components by the 12 eigenmodes with $k = 0$–2 and $n = 1$–4. Figure 6 gives the corresponding local fractional contributions to the Reynolds shear stress. The contributions of these 12 modes to the total energy are about 50%, but this is divided between a large contribution to streamwise kinetic energy of about 60% for $y/h = 0.05$–0.6, and a much smaller contribution to the wall-normal kinetic energy of about 20% for $y/h > (0.1$–$0.2)$. Thus, most of the streamwise kinetic energy below $y/h = 0.6$ is large-scale, but the strong majority of the wall-normal kinetic energy is smaller-scale. In the channel centre, contributions to both components are approximately equal. These results are consistent with the observation that smaller numbers of the large-scale structures reach the centreline. In contrast, figure 6 shows that $\overline{uv}$ receives strong contributions from large scales at the centreline. This suggests that the Reynolds stress events are intermittent in the region of the centreline.

The local contributions of the 12 eigenmodes with $k = 0$–2 and $n = 1$–4 to the local Reynolds stress are 60–80%, except for the region close to the wall (figure 6). This
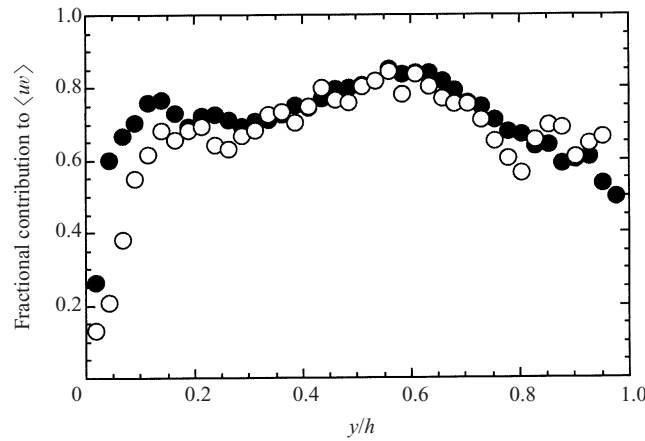
FIGURE 6. Profiles of the fractional contributions of the first 12 eigenmodes ($k = 0$–$2, n = 1$–4) to the Reynolds shear stress. Solid symbols, $Re_h = 5378$; open symbols, $Re_h = 29\,935$.

implies that the low mode (large-scale) motions are quite energetic and not 'inactive' in generating turbulence above the buffer layer. In the near-wall region, the contributions of the large-scales are much smaller. Because of the limited spatial resolution of the measurements relative to the scales in this region, the values shown in figures 5 and 6 are only estimates of the precise contributions. Even so, the fractional contribution to the near-wall Reynolds shear stress lies in a range of 13–26%. This is not inconsistent with an estimate of 15% by Naguib & Wark (personal communication 1999).

4.3. *Velocity fields of the large-scale flows*

We turn now to the question of determining the flow patterns associated with the large-scale energetic modes. To be specific, we shall seek the structure of the flows that create the contributions from the first twelve modes, containing about half of the kinetic energy, and two-thirds of the Reynolds shear stress. The individual eigenfunctions cannot, by themselves, describe the structure of an eddy, because eddies are composed of many modes. This is especially clear for homogeneous turbulence in which the eigenfunctions are simple trigonometric waves. Lumley's (1970) characteristic eddy method attempts to define a single characteristic eddy by projecting the modal structure on a shot noise model of randomly scattered eddies, but this approach suffers from a fundamental ambiguity in which the phases of the complex eigenfunctions are left undetermined (Moin & Moser 1989). This problem does not arise if we simply phrase the question as one of determining the structure of the eddies that contribute to certain groups of modes, for then the phases of each mode are found directly by projecting the instantaneous velocity fields onto the group. For the present work, this approach is particularly appropriate, because we have already identified the group of modes that is of interest. Of course, other groups of modes could also be identified, but they would be associated with different questions.

4.3.1. *Vector structure of the modes*

   Although individual modes cannot fully describe an eddy, the structure of each mode is of interest, nonetheless, as a component of the complete structure. From equation (11), the part of the fluctuating velocity component that is associated with

the (k, n) mode is

$$u_i^{(k,n)}(x, y) = \operatorname{Re} a^{(k,n)} \operatorname{Re} \psi_i^{(k,n)}(x, y) - \operatorname{Im} a^{(k,n)} \operatorname{Im} \psi_i^{(k,n)}(x, y). \quad (18a)$$

(The imaginary part of (11) must vanish, since u_i is real.) It is easy to show that the vectors for the imaginary eigenfunctions are the real eigenfunction vectors $\psi_i^{(k,n)} = (\psi_1^{(k,n)}, \psi_2^{(k,n)})$ with a $\frac{1}{2}\pi$ phase shift, corresponding to a dimensional spatial shift of $L_x/4k$. Then, the (k, n) mode component of the velocity is

$$u_i^{(k,n)}(x, y) = \operatorname{Re} a^{(k,n)} \operatorname{Re} \psi_i^{(k,n)}(x, y) - \operatorname{Im} a^{(k,n)} \operatorname{Re} \psi_i^{(k,n)}(x - L_x/4k, y). \quad (18b)$$

The eigenfunctions can be presented in a vector form, since the two components ψ_1 and ψ_2, are related to velocity components u_1 and u_2. A real eigenfunction vector can be defined as

$$\operatorname{Re} \psi^{(k,n)}(x, y) = (\operatorname{Re} \psi_1^{(k,n)}(x, y), \operatorname{Re} \psi_2^{(k,n)}(x, y)), \quad (19a)$$

$$= (\operatorname{Re}[\phi_1^{(k,n)}(x, y) e^{j2\pi kx}], \operatorname{Re}[\phi_2^{(k,n)}(x, y) e^{j2\pi kx}]). \quad (19b)$$

From (18b), the modal velocity can be constructed from a linear combination of the vector field of the real eigenfunction and the vector field of the real eigenfunction shifted by $1/4k$. Thus, it suffices to consider the vector fields given by equation (19).

Figure 7 presents the real eigenfunction vector fields for eigenmodes $k = 0$ and 1 with $n = 1, 2$ and 3 for $Re_h = 5378$. Every other vector has been removed to show the patterns more clearly. Because of homogeneity in the streamwise direction, the structure of each eigenfunction is sinusoidal with phase $\theta(x) = 2\pi kx$. The structure in the inhomogeneous wall-normal direction is determined by the wall-normal eigenfunctions, $\phi_i^{(k,n)}(y)$, cf. equation (19b) and figure 3. Recall that the eigenfunction vectors of the $k = 0$ modes represent the projection of all modes having wavelengths longer than the fundamental wavelength of the domain, 3.2h. They are independent of x, but the projected wall-normal component does not vanish, so the $k = 0$ modes still contribute to the Reynolds shear stress. The $(0, 1)$ and $(0, 3)$ modes are symmetric with respect to the centreline, while the $(0, 2)$ mode is antisymmetric.

The eigenfunction vector fields of the $k = 1$ modes in figure 7 are once-periodic in 3.2h. They show motions like ejections (second-quadrant Q2 events) and sweeps (fourth-quadrant Q4 events) that are strong in a region inclined at about 35° to the wall. These motions contribute positively to the net mean Reynolds shear stress, the amount depending on the phase relationship between the u- and v-eigenfunctions. In figures 7(d) and 7(f), we can discern a recurring pattern consisting of an inclined Q2 event (along the locus of the straight line) in the lower half of the channel lying under a clockwise rotating motion (highlighted by the ellipse), and an inclined Q4 event lying under a counterclockwise rotating motion (highlighted by the second ellipse). The Q2 and Q4 flows create between them a stagnation point and an associated inclined shear layer. The combination of a rotation about the spanwise direction, an inclined region of Q2 vectors with a local maximum Q2 event and the shear layer created by a weaker upstream Q4 event has been identified by Adrian *et al.* (2000) as the signature of a flow pattern that carries large amounts of Reynolds shear stress and occurs frequently in turbulent boundary layers. They defined this pattern as the *hairpin vortex signature*, arguing that it corresponds to the flow in the central (x, y)-plane of a hairpin-like vortex inclined in the streamwise direction. The general sense of the hairpin paradigm included hairpin, horseshoe and cane-like structures having the general shape of a quasi-streamwise leg of concentrated vorticity inclined
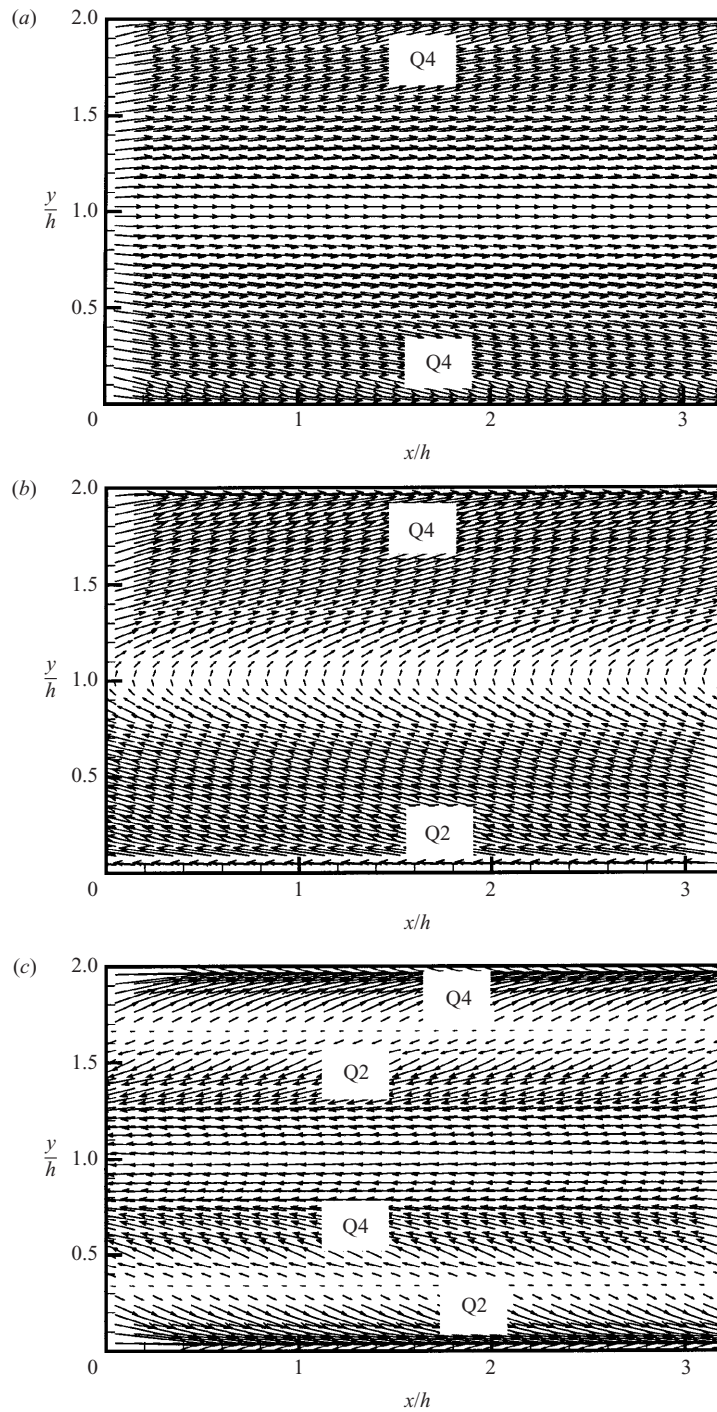
Z. Liu, R. J. Adrian and T. J. Hanratty

FIGURE 7 (*a–c*). For caption see facing page.

to the wall and turning over in the spanwise direction near its top (to account for the spanwise vortex observed in the (x, y)-plane). The Q2 events with local maxima were associated with vortex induction of the head and legs of the hairpin.

Since the purpose of the present paper is not to determine the relevance of the
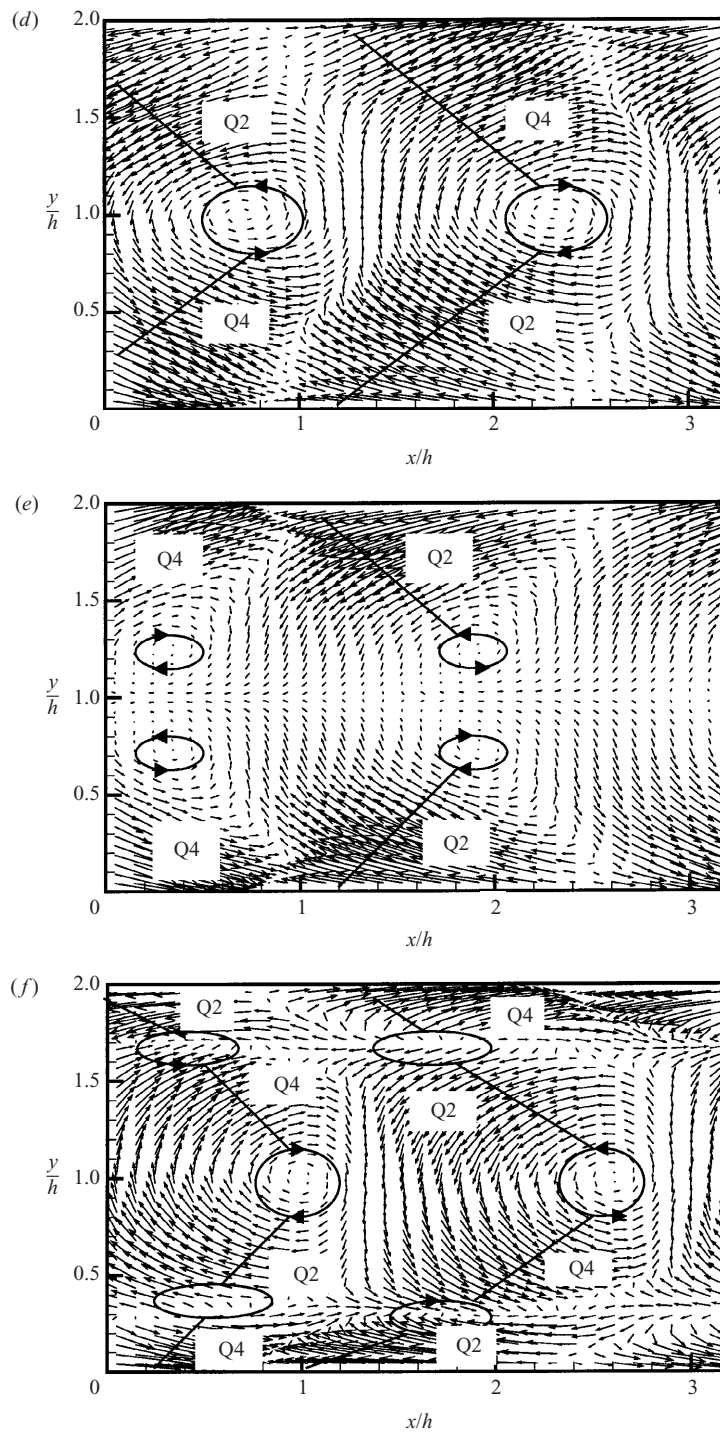
FIGURE 7. The eigenfunction vector fields of the first 6 most energetic modes for $Re_h = 5378$. Mode order: (*a*) $(k, n) = (0, 1)$; (*b*) $(k, n) = (0, 2)$; (*c*) $(k, n) = (0, 3)$; (*d*) $(k, n) = (1, 1)$; (*e*) $(k, n) = (1, 2)$; (*f*) $(k, n) = (1, 3)$.
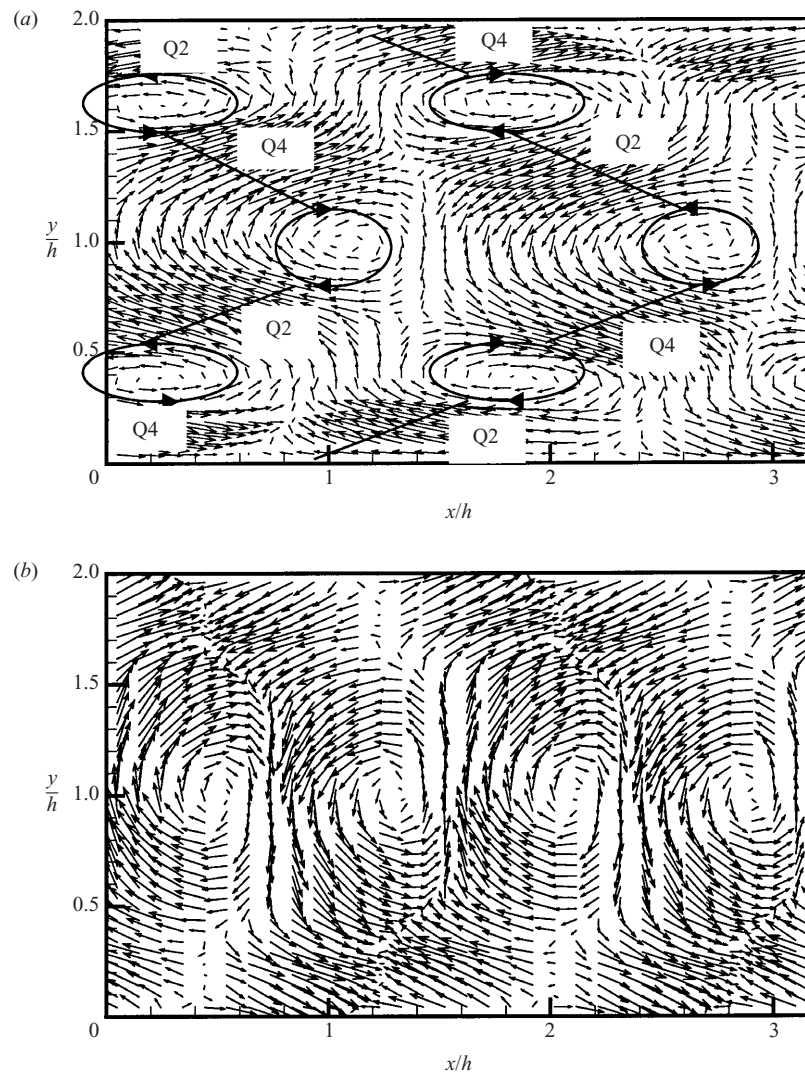
FIGURE 8. The eigenfunction vector fields for $Re_h = 29\,935$ with mode order:
(a) $(k, n) = (1, 3)$; (b) $(k, n) = (2, 2)$.

hairpin paradigm to the POD modes, we shall refer to the flow pattern described above as the 'signature of a characteristic Reynolds stress event'.

Note that the reflectional symmetry with respect to the centreline in figure 7(*e*) results in regions of inclined Q2 and Q4 events that do not lie under a transverse vortex. Instead, the pattern looks like an in-plane convergence toward a three-dimensional saddle point with out-of-plane flow.

The eigenvector fields of the $Re_h = 29\,935$ flow are very similar to those in figure 7 for $Re_h = 5.378$. One pattern, a $(3, 1)$ mode presented in figure 8(*a*), demonstrates the similarity that is typical of the other modes. The higher-order $(2, 2)$ mode in figure 8(*b*) illustrates the increased layering that occurs in the *y*-direction as the modal order increases.

Order	$Re_h = 5378$			$Re_h = 29\,935$		
(k, n)	$\alpha^{(k,n)}$	$\|a^{(k,n)}\|$	$\sqrt{\lambda}^{(k,n)}$	$\alpha^{(k,n)}$	$\|a^{(k,n)}\|$	$\sqrt{\lambda}^{(k,n)}$
$(0, 1)$	0	0.271	0.522	0	2.430	0.621
$(0, 2)$	0	0.280	0.482	0	1.820	0.504
$(0, 3)$	0	0.450	0.273	0	1.210	0.269
$(0, 4)$	0	0.453	0.262	0	1.860	0.232
$(1, 1)$	-0.973	0.414	0.370	-0.240	0.466	0.404
$(1, 2)$	-0.123	0.102	0.368	-1.320	2.880	0.369
$(1, 3)$	-0.641	0.244	0.303	-1.240	1.150	0.303
$(1, 4)$	-0.853	0.284	0.248	-0.567	0.692	0.250
$(2, 1)$	-0.423	0.216	0.249	1.170	0.775	0.238
$(2, 2)$	-1.320	0.079	0.211	0.914	0.566	0.226
$(2, 3)$	0.913	0.145	0.183	0.618	0.574	0.191
$(2, 4)$	0.651	0.122	0.175	-1.050	0.098	0.162

TABLE 5. The phases, $\alpha^{(k,n)}$, and amplitudes, $|a^{(k,n)}|$, of the weighting coefficients, $a^{(k,n)}$, used in the projections of the two sample instantaneous realizations in figures 9(a) and 10(a) onto 12 eigenmodes for the two Reynolds numbers. The square roots of the corresponding eigenvalues are given for comparison.

4.3.2. *Velocity fields of the energetic, large-scale motion*

To sample the types of eddy structures that are characterized by the low-order eigenmodes, we have projected many snapshots of instantaneous fluctuating flow fields onto the subspace spanned by the 12 eigenmodes ($k = 0$–2, $n = 1$–4). Representative samples of the random velocity fields taken from the data sets for each Reynolds number are shown in figures 9(a) and 10(a). The corresponding projected flow fields are displayed in figures 9(b) and 10(b). This procedure would fail to yield a clear picture of the eddies characterized by these modes if no such eddies were present in the sample realizations. However, table 5 shows that the magnitudes of the Fourier coefficients $|a^{(k,n)}|$ of each projection are comparable to the root-mean-square values, as given by the square root of the eigenvalues. Therefore, eddies that are typical of the first 12 modes are not sparse, so they are usually present in an individual sample. (The phases of the Fourier coefficients for each random realization are different, reflecting the dynamical behaviour of the eigenmodes.) The projected fields in figures 9(b) and 10(b) each clearly contain two structures that possess all of the elements of the signature of a characteristic Reynolds stress event, as described above. A Q2 ejection of fluid from the wall with length scale of at least 500 viscous wall units (1.6h) in the streamwise direction and a strong Q4 motion of fluid from the outer region of the channel can be seen in the lower half of figure 9(b) for the lower Reynolds number. The Q2 and Q4 motions meet each other and generate a stagnation point/shear layer that extends from $y^+ = 100$ to 200 with an inclination angle of about $30°$ to $40°$ to the wall, in a manner very similar to that discussed above for the eigenmodes. A similar pattern coming down from the top wall appears to provide the Q4 motion for the downstream eddy on the lower wall.

The scales of the patterns in figure 9(b) are of the order of the channel height, but this is not very large in terms of the viscous length scale at the lower Reynolds number. The projection of the higher Reynolds number velocity field in figure 10(b) offers much more convincing evidence that these structures do scale with the outer
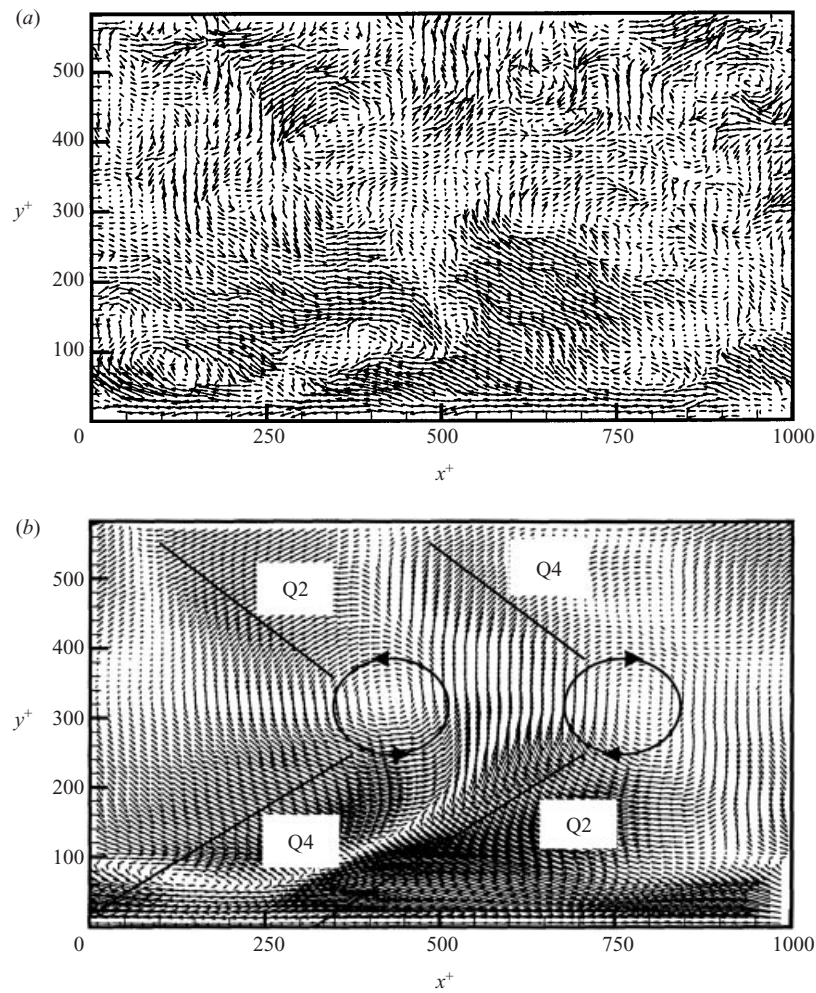
FIGURE 9. (*a*) An instantaneous turbulent fluctuating velocity field from PIV measurements at $Re_h = 5378$. (*b*) The projection onto the first 12 eigenmodes ($k = 0$–$2, n = 1$–4).

length scale. Two signatures of large-scale characteristic stress events can be seen, one attached to the bottom wall and one attached to the top wall. To demonstrate further the similarity between large eddies at high and low Reynolds numbers, a second $Re_h = 29\,925$ field is projected onto the lowest 12 modes in figure 10(*c*). This random snapshot is remarkably similar to the field in figure 9(*b*). The streamwise scales of the large motions exceed 2000 viscous wall units, about $2h$, and their vertical size is about one channel half-height or $h^+ = 1414$. Projection onto the first 6 modes instead of the first 12 modes has no qualitative effect and relatively little quantitative effect on the pattern of the vector fields. Examination of the full data sets reveals that projections containing patterns that meet all of the criteria for the signature of a characteristic stress event occur over half of the time. Given that the eddies have random spanwise locations relative to the fixed plane of the PIV data, the high frequency with which the signatures are observed indicates that these structures are indeed characteristic of the large-scale fields.
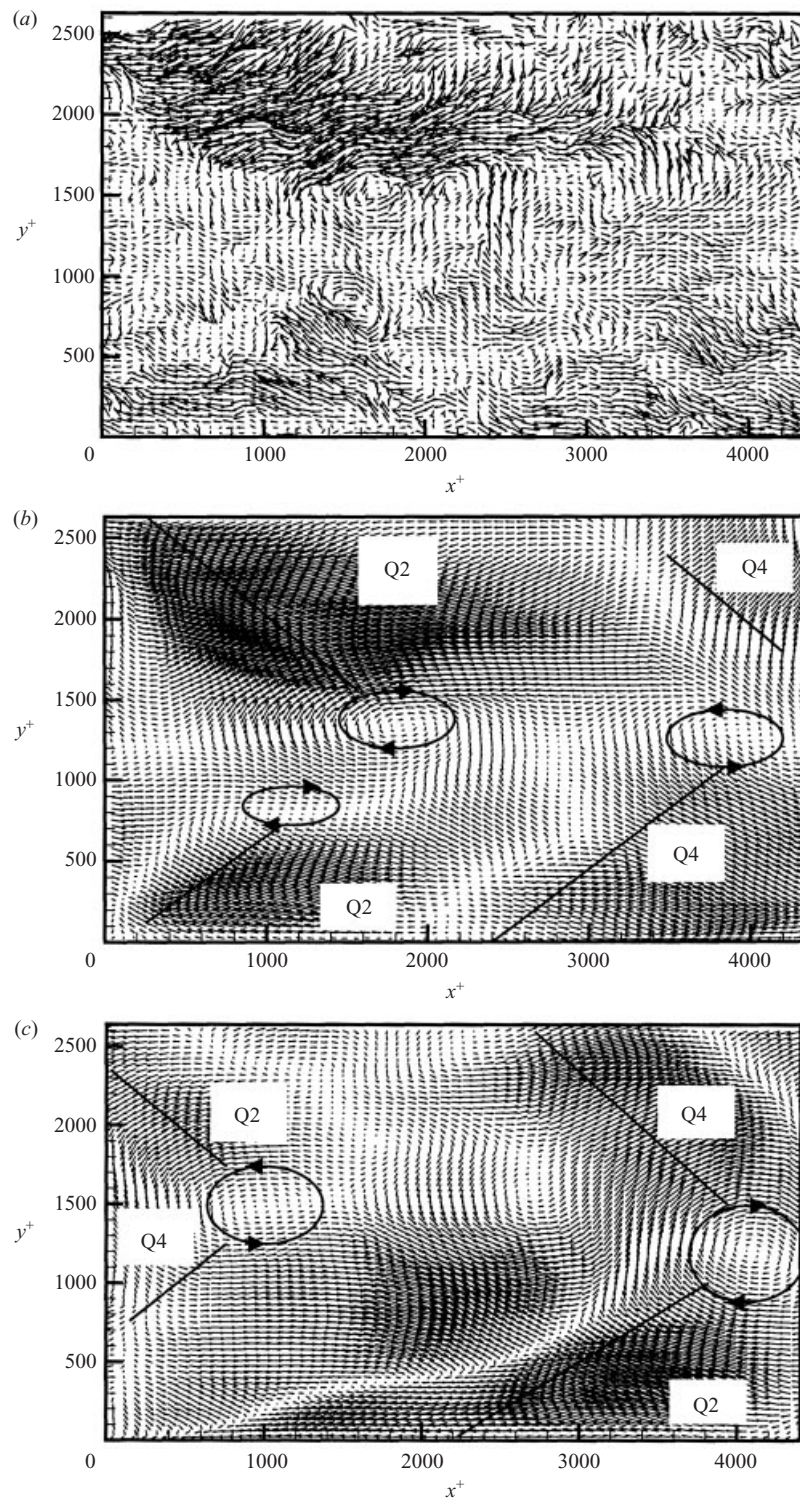
(a)

(b)

(c)

FIGURE 10. (a) An instantaneous turbulent fluctuating velocity field from PIV measurements at $Re_h = 29\,935$. (b) The projection onto the first 12 eigenmodes ($k = 0$–$2, n = 1$–4). (c) The projection of another flow field onto the same first 12 eigenmodes ($k = 0$–$2, n = 1$–4).

5. Conclusions

Turbulent flow fields in the outer region of flow through a rectangular channel at $Re_h = 5378$, and $Re_h = 29\,935$ have been measured in the streamwise-wall-normal plane and analysed by two-dimensional proper orthogonal decomposition. The scaling of the outer flow structures was found to be only approximately the same for the two Reynolds numbers. The measurements at the larger Reynolds number reveal a slightly larger contribution to the shear stress from smaller scale motions. This can be seen by comparing the eigenmodes in tables 3 and 4 and the correlation functions in figures 1 and 2.

There are two principal results. First, the low-order eigenmodes that carry much of the turbulent kinetic energy are large-scale motions having wavelengths equal to or longer than $3.2h$. Second, these large-scale motions also carry most of the Reynolds stress. The 6 eigenmodes (0–2, 1–2), carry 33% of the energy and 56% of the Reynolds shear stress at $Re_h = 5378$; they carry 37% of the energy and 50% of the Reynolds shear stress at $Re_h = 29\,935$. The inclusion of 6 additional modes $[(2, 1), (1, 3), (2, 2), (1, 4), (2, 4), (0, 4)]$ captures 48% and 50% of the energy for the two Reynolds numbers, respectively, and 67% and 75% of the respective Reynolds shear stresses. At low Reynolds number the turbulent spectrum is relatively narrow, so there is little difference between the scales of the largest and smallest structures. Hence, the fact that the first few modes carry much of the Reynolds stress is not surprising. For example, in the flow studied by Moin & Moser (1989) $h^+ = 180$, and the small-scale motions having length of order 100 viscous units are of the same size as those spanning the channel. At Reynolds number of 5378, and most especially at 29 935, the large scales truly are much larger than the small scales, e.g. $h^+ = 1414$. Hence, the low modes are very large, and it is surprising that they carry so much Reynolds stress. That the large-scale motions are highly active in the transport of streamwise momentum implies that the Reynolds stresses are far from being a local phenomenon, which has significant ramifications regarding the modelling of the Reynolds shear stress using Boussinesq eddy viscosity or other gradient transport models. It is interesting to note that a discussion of the possibility of large-scale motions constituting an important transport mechanism can be found in Hinze (1975).

At both Reynolds numbers, the energy associated with the normal velocity is carried by motions that are significantly smaller than the scale of the largest streamwise motions. For example, at the higher Reynolds number, the streamwise motions extend to at least 2–$4h$, while the largest wall-normal motions extend to $0.3h$. Since the Reynolds shear stress is also carried by the large-scale u-components flows, this implies that the v-component of the flows associated with Reynolds shear stress is not very energetic. At first thought, it is difficult to imagine a turbulent motion whose u-component extends over a region much longer than that of the v-component. One such motion is the vortex packet discussed by Adrian *et al.* (1998, 2000). It consists of long regions of coherently aligned hairpin-like eddies. The largest of the individual eddies reach a significant fraction of the layer thickness, about $0.5h$, and the length of the packets reaches 2–$4h$. Within a packet, the individual eddies coherently induce a region of negative streamwise momentum, which, because of their coherent alignment becomes a negative u-fluctuation almost as long as the packet. The induced flow is nearly parallel to the wall, i.e. it has little v-energy. Thus, within an individual eddy the u- and v-components may have similar scale, but the assembly of them has a much longer scale. The short v-correlation is associated with individual eddies; while the long u-correlation is associated with the coherent induction of many aligned eddies.

A comparison of the eigenmodes with actually observed flow fields shows that individual modes do not represent eddy structures. Their contributions to the flow field are best seen by projecting instantaneous realizations of the flow onto the eigenmodes. By doing this for the first 12 modes, which contain half of the kinetic energy, it is found that large structures have a signature in the (x, y)-plane that has been identified herein as the signature of a characteristic Reynolds stress event. These projected patterns have sizes of the order of the channel height, and they are similar to the signature of a hairpin vortex.

Lastly, the streamwise extent of the longest scales in this study must be interpreted as 3.2*h or longer*. Recent studies in pipe flow of the one-dimensional power spectrum of the streamwise velocity (Kim & Adrian 1999; Hommema 2001) and the uv co-spectrum (Hommema 2001) show that modes larger than 10 pipe radii contribute substantially to the total mean values. Similar behaviour could occur in channel flow.

REFERENCES

ADRIAN, R. J. 1991 Particle-imaging techniques for experimental fluid mechanics. *Ann. Rev. Fluid Mech.* **23**, 261–304.

ADRIAN, R. J., BALACHANDAR, S. & TOMKINS, C. D. 1998 The structure of vortex packets in wall turbulence. *AIAA Paper* 98-2962.

ADRIAN, R. J. & LEKAKIS, I. C. 1991 A scale-gap in the structure of moderate Reynolds number turbulent pipe flow. *Bull. Am. Phys. Soc.* **36**, 2698.

ADRIAN, R. J., MEINHART, C. D. & TOMKINS, C. D. 2000 Organization of vortical structure in the outer region of the turbulent boundary layer. *J. Fluid Mech.* **422**, 1–51.

BAKEWELL, H. P. & LUMLEY, J. L. 1967 Viscous sublayer and adjacent wall region in turbulent pipe flow. *Phys. Fluids* **10**, 1880–1889.

CHAMBERS, D. H., ADRIAN, R. J., MOIN, P., STEWART, D. S. & SUNG, H. J. 1988 Karhunen–Loève expansion of Burger's model of turbulence. *Phys. Fluids* **31**, 2573–2582.

GRANT, H. L. 1958 The large eddies of turbulent motion. *J. Fluid Mech.* **4**, 149–190.

GUENTHER, A., PAPAVASSILIOU, D. V., WARHOLIC, M. D. & HANRATTY, T. J. 1998 Turbulent flow in a channel at low Reynolds numbers. *Exps. Fluids* **25**, 503–511.

HANRATTY, T. J., ADRIAN, R. J., LIU, Z.-C., BROOK, J., PAPAVASSILIOU, D., MCLAUGHLIN, J. 1993 Recent results on the structure of wall turbulence. In *Proc. Ninth Symp. Turbulent Shear Flows*, Kyoto, pp. 11.3.1–11.3.3.

HERZOG, S. 1986 The large-scale structure in the near-wall region of turbulent pipe flow. PhD thesis, Cornell University.

HINZE, J. 1975 *Turbulence*, 2nd Edn, p. 579. McGraw-Hill.

HOMMEMA, S. E. 2001 Very-large-scale motions in wall-bounded turbulent flows. PhD thesis, University of Illinois, Urbana-Champaign.

KIM, K. C. & ADRIAN, R. J. 1999 Very large-scale motion in the outer layer. *Phys. Fluids* **11**, 417–422.

KLINE, S. J., REYNOLDS, W. C., SCHRAUB, F. A. & RUNSTADLER, P. W. 1967 The structure of turbulent boundary layers. *J. Fluid Mech.* **30**, 741–773.

KOVASZNAY, L. S. G., KIBENS, V. & BLACKWELDER, R. F. 1970 Large-scale motion in the intermittent region of a turbulent boundary layer. *J. Fluid Mech.* **41**, 283–325.

LEE, M. J. & KIM, J. 1991 The structure of turbulence in a simulated plane Couette flow. In *Proc. Turbulent Shear Flow Symp.* Munich, 9–11 September, pp. 5.3.1–5.3.6.

LEKAKIS, I. C. 1988 Coherent structure in turbulent pipe flow. PhD thesis, University of Illinois, Urbana.

LIU, Z.-C., ADRIAN, R. J. & HANRATTY, T. J. 1994 Reynolds-number similarity of orthogonal decomposition of the outer layer of turbulent wall flow. *Phys. Fluids* **6**, 2815–2819.

Liu, Z.-C., Adrian, R. J. & Hanratty, T. J. 1995 A study of turbulent channel flow with 2-D proper orthogonal decomposition. *Bull. Am. Phys. Soc.* **40**, 2014.

Liu, Z.-C., Landreth, C. C., Adrian, R. J. & Hanratty, T. J. 1991 High resolution measurement of turbulent structure in a channel with particle image velocimetry. *Exps. Fluids* **10**, 301–312.

Lu, J. L. & Smith, C. R. 1991 Velocity profile reconstruction using orthogonal decomposition. *Exps. Fluids* **11**, 247–254.

Lumley, J. L. 1970 *Stochastic Tools in Turbulence*. Academic.

Moin, P. & Moser, R. D. 1989 Characteristic-eddy decomposition of turbulence in a channel. *J. Fluid Mech.* **200**, 471–509.

Moser, R. D. 1994 Kolmogorov inertial range spectra for inhomogeneous turbulence. *Phys. Fluids* **6**, 794–801.

Murlis, J., Tsai, H. M. & Bradshaw, P. 1982 The structure of turbulent boundary layers at low Reynolds numbers. *J. Fluid Mech.* **122**, 13–56.

Naguib, A. M. & Wark, C. E. 1992 An investigation of wall-layer dynamics using a combined temporal filtering and correlation technique. *J. Fluid Mech.* **243**, 541–560.

Niederschulte, M. A., Adrian, R. J. & Hanratty, T. J. 1990 Measurements of turbulent flow in a channel at low Reynolds numbers. *Exps. Fluids* **9**, 222–230.

Papavassiliou, D. V. & Hanratty, T. J. 1997 Interpretation of large-scale structures observed in a turbulent plane Couette flow. *Intl J. Heat Fluid Flow* **18**, 55–69.

Robinson, S. K. 1991 *The Kinematics of Turbulent Boundary Layer Structure*. NASA TM-103859.

Sirovich, L., Ball, K. S. & Handler, R. A. 1991 Propagating structures in wall-bounded turbulent flows. *Theoret. Comput. Fluid Dyn.* **2**, 307–317.

Sirovich, L., Ball, K. S. & Keefe, L. R. 1990 Plane waves and structures in turbulent channel flow. *Phys. Fluids* A **2**, 2217–2226.

Sung, H. J. & Adrian, R. J. 1994 Karhunen–Loève expansion of the derivative of an inhomogeneous process. *Phys. Fluids* **6**, 2233–2235.

Townsend, A. A. 1958 The turbulent boundary layer. In *Boundary Layer Research. Proc. IUTAM Symp.* Freiburg, 26–29 August 1957, pp. 1–15. Springer.

Townsend, A. A. 1976 *The Structure of Turbulent Shear Flow*, 2nd edn. Cambridge University Press.

Warholic, M. D. 1997 Modification of turbulent channel flow by passive and additive devices. PhD thesis, University of Illinois, Urbana-Champaign.

Wygnanski, I. J. & Champagne, F. H. 1973 On transition in a pipe. Part 1. The origin of puffs and slugs and the flow in a turbulent slug. *J. Fluid Mech.* **59**, 281–335.